particles

MDPI

Article

Techniques for Reconstruction of Strange Objects at MPD

Alexander Zinchenko

Joint Institute for Nuclear Research, Joliot-Curie 6, 141980 Dubna, Moscow Region, Russia; Alexander.Zinchenko@jinr.ru

Abstract: Study of the strangeness production in heavy-ion collisions is one of the most important parts of the physics program of the MPD experiment at the NICA collider. Therefore, the problem of a reliable and efficient reconstruction of strange objects should be addressed with a high priority during the preparation to the experiment. The paper describes the approach to this task which was developed and implemented as a part of the MPD software. Some results of its application during the detector Monte Carlo feasibility studies are presented.

Keywords: heavy-ion collisions; strangeness production; vertex reconstruction; decay reconstruction

Citation: Zinchenko, A. Techniques for Reconstruction of Strange Objects at MPD. *Particles* **2021**, *4*, 178–185. https://doi.org/10.3390/particles4020016

Academic Editor: Peter Senger

Received: 9 March 2021
Accepted: 19 April 2021
Published: 21 April 2021

1. Introduction

The experimental investigation of the high-density nuclear matter equation of state is an important subject for present and future research with heavy-ion beams. The Nuclotron-based Ion Collider Facility (NICA), which is currently under construction at the Joint Institute for Nuclear Research (JINR) in Russia [1], offers unique possibilities to produce baryonic matter at high densities. The Multi-Purpose Detector (MPD) at the NICA collider [2] is designed and being assembled to measure different probes, which will provide new information on the quantum chromodynamic (QCD) phase diagram at large baryon-chemical potentials, including the high-density equation-of-state (EOS).

Strangeness production is of particular interest at energies available at NICA ($\sqrt{s_{NN}}$ = 4–11 GeV). For instance, some theoretical models predict that an enhancement of the strangeness production in heavy-ion collisions experimentally observed at SPS [3] and RHIC [4] in this energy range can be explained by the deconfinement phase transition, when multiple $s - \bar{s}$ pairs are created via gluon fusion reactions, resulting in a higher yields of strangeness compared to that from a hadron gas scenario [5]. However, there are some alternative explanations of such an enhancement not requiring formation of the quark–gluon plasma [6]. Study of the yield of multi-strange hyperons at NICA energies can provide information on the onset of a phase transition from nuclear to quark matter expected during the evolution of a neutron star merger with a total mass of 2.8 solar masses, when a density between 3 and 4 nuclear matter saturation densities ρ_0 and at a temperature of about 50 MeV is reached [7].

Relativistic heavy-ion collisions, where many strange particles (kaons and hyperons) are produced, offer a unique possibility to create exotic nuclear objects with strangeness—hyper-nuclei [8]. The mechanism and dynamics of hypernuclei formation is not well understood—several approaches are suggested to explain their production rates: coalescence of lambdas with nucleons at midrapidity [9], thermal models [10], or absorption of some of the produced hyperons by the residual spectator nuclei [11]. The energy range of the NICA research program covers the region of the maximal baryon density where the production rates of nuclear clusters with strangeness are predicted to be considerably enhanced allowing a detailed study of their production mechanism.

Short-lived strange objects such as resonances can also serve as an important instrument to study properties of the hot and dense nuclear matter. In particular, they are

sensitive to the rescattering and regeneration processes occurring between the chemical and the kinetic freeze-out in heavy-ion collisions, as well as to some other phenomena [12].

In order to better understand the dynamics of hot and dense hadronic matter, in particular, the strangeness production mechanism, the Multipurpose Detector (MPD) experiment at the NICA collider, will provide new precise experimental data on the total yields, rapidity, transverse momentum, and azimuthal angle distributions of strange particles, including (anti)-hyperons and hypernuclei. However, to do so, the experiment will have to develop and implement the software methods and tools to reconstruct strange objects and extract necessary information. The current status of such an activity is presented below.

2. MPD Detector Configuration

The Multi-Purpose Detector at the NICA collider has been designed to detect hadrons, electrons, and photons over a large phase-space at the high event rate achieved at NICA. At the designed luminosity of $L = 10^{27}$ cm^{-2}s^{-1} for Au + Au, the collision rate will be $\sim$7 kHz.

Figure 1 shows a three-dimensional view of the MPD setup. All the subdetectors are located inside a superconducting solenoid, which produces a magnetic field along the beam axis with a nominal strength of 0.5 T. The MPD Time-Projection Chamber (TPC) is the main tracking device for the reconstruction of charged particle trajectories over the pseudorapidity range of $|\eta| < 1.5$. It will provide the momentum measurement for charged particles with a precision better than 3.5% at transverse momentum p_T below 2 GeV/c and particle identification via the specific energy loss measurement (dE/dx) in the TPC gas with a resolution better than 8%. Track reconstruction quality outside the midrapidity region will be enhanced by a straw-tube End Cap Tracker (ECT). The Inner Tracker (IT) system made of several layers of silicon pixel detectors is intended for a very precise determination of the position of primary and secondary vertices. The Time-of-Flight (TOF) system, located just outside the TPC and built of Multi-gap Resistive Plate Chamber (MRPC), is meant for identifying charged particles in the intermediate momentum region, where the TPC can not discriminate hadrons by dE/dx measurements. With the overall TOF timing resolution of about 80 ps, a π/K separation greater than 3σ up to 1.2 GeV/c and K/p separation up to 2.5 GeV/c will be achieved. The primary purpose of a segmented Electromagnetic Calorimeter (ECAL), built of about 38,000 modules of the "shashlyk" lead-scintillator type, is to measure the spatial position and energy of photons and to improve identification of electrons. The MPD Forward Detector (FD) consisting of two arrays of quartz Cherenkov detectors capable of registering high energy photons and relativistic charged particles with the 40 ps time resolution will provide fast timing and triggering signals to the experiment. Two arms of the Forward Hadron Calorimeters (FHCAL), each made of 44 lead-scintillator modules, cover the pseudorapidity range $2.8 < |\eta| < 4.5$. The information from FHCAL about the forward going energy distribution will be used for the centrality determination and event plane analysis.

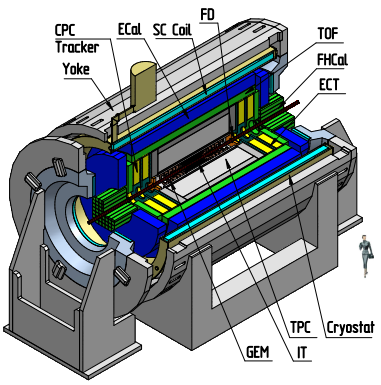

Figure 1. Three-dimensional view of the MPD detector.

It is planned to put MPD in operation in two stages. The end-cap detector parts and subdetectors as well as the Inner Tracker will be added at the second stage. More detailed description of the MPD detector can be found in Ref. [13].

3. Reconstruction of Decays

Strange objects are found by making use of their decay topology and/or the invariant mass of their decay products. Figure 2 shows schematic views of the decay topology of Λ and Ω hyperons in the bending plane of the magnetic field. Decays of long-lived particles can be selected using the secondary vertex reconstruction technique, based on finding decay vertices decoupled from the primary one (interaction point). In order to reject wrong track combinations with primary tracks in such topologies, special cuts are applied on the minimum value of the impact parameters to the primary vertex $dca_{K,p,\pi}$. Next, the track combination is rejected if the distance of the closest approach dca_{V0} in space between the daughter track candidates is larger than a given value. This cut ensures that the decay tracks originate from the same object and can also be applied for a short-lived particle decay search. To further suppress mostly primary track combinations, it is also required that the secondary vertex position should be at a certain distance *path* from the primary one. The topology reconstruction quality can also be enforced by requiring the impact-parameter of the decayed particle with respect to the primary vertex or its pointing angle, defined as the angle between its momentum and the direction vector from the primary to the secondary vertex, to be smaller than a given value. Finally, the invariant mass is calculated under the proper daughter particle hypotheses, e.g., a proton and a pion for the case of V0 or Λ and a kaon for Ω hyperon.

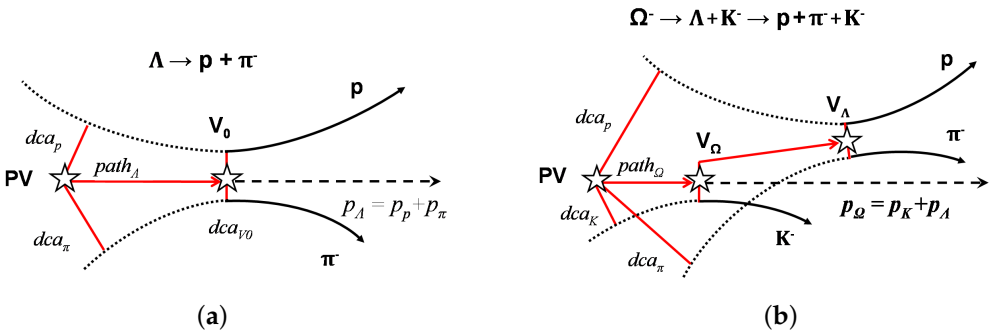

Figure 2. (**a**) Event topology of two-particle decays of a neutral particle (e.g., $\Lambda \rightarrow p + \pi^-$); (**b**) event topology of cascade-type decays (e.g., $\Omega^- \rightarrow \Lambda + K^- \rightarrow p + \pi^- + K^-$) (transverse view). Here, dca_p, dca_π, and dca_K are the distances of the closest approach of the decay tracks to the primary vertex PV, dca_{V0} is the distance between daughter tracks in the decay vertex V_0, *path* is the decay length, $\mathbf{p}_p$, $\mathbf{p}_\pi$, $\mathbf{p}_K$, $\mathbf{p}_\Lambda$, and $\mathbf{p}_\Omega$ are momenta of particles.

The decay reconstruction package is built around a vertex fitting procedure based on the Kalman filtering technique [14]. The task of the secondary vertex reconstruction and decay product fitting deals with particle parameters. Therefore, for reasons of the software development efficiency and software modularity requirement, it can be decoupled from the track reconstruction task. This approach makes it possible to be independent of the detector geometry and to more easily include tracks from future subdetectors, as well as to treat charged and neutral objects on the same footing. It is also a "natural" step because of the necessity to change the track parameterization near the origin of the coordinate system, where the particle decays usually take place. Within the object-oriented approach realized in the MpdRoot software framework [15], it required introducing a separate analysis-oriented object MpdParticle with its respective methods, which is created from reconstructed tracks or other MpdParticles (both charged and neutral) and fulfills the above-mentioned conditions. Such a concept was inspired by a so-called KF Particle of the CBM experiment [16] and the approach developed for the BaBar experiment [17].

4. Results

The strange particle reconstruction procedure described above has been extensively used for MPD Monte Carlo feasibility studies [18–21] with different event generators, describing heavy-ion collisions [22–24]. The exact values of selection cuts were found by performing a multidimensional scan over the whole set of selection criteria with a requirement to maximize the invariant mass peak significance. The significance is defined as $S/\sqrt{S+B}$, where S and B are the total numbers of signal and background combinations inside the $\pm 2\sigma$ interval around the peak position, obtained from a fit of the invariant mass distribution to a sum of Gaussian and polynomial functions with σ being the Gaussian width parameter (Figure 3). The corresponding scan procedure was realized using multiple loops over selection criteria in some steps, giving the invariant mass peak significance for each set of selection cut values. The maximum significance point defined the set of cuts chosen to produce final results. It was also found that both the DCA and two-track separation cuts were more efficient if applied in χ^2-space, i.e., if normalized to their respective errors.

Figure 3 shows reconstructed invariant mass spectra for Λ, $\overline{\Lambda}$ and Ξ^- hyperons, obtained for different event numbers from PHSD [24] simulation of minimum bias Au+Au collisions at $\sqrt{s_{NN}} = 11$ GeV. One can see clear peaks with high signal/background ratios, obtained with reasonable selection efficiencies. Figure 4 demonstrates that the MPD detector provides a uniform coverage for hyperons at midrapidity. Figure 5 demonstrates how Λ hyperons can be selected in different p_T-intervals, which is necessary, e.g., when reconstructing p_T-spectra. More rare multistrange (anti)hyperons $\overline{\Xi}^+$, Ω^- and $\overline{\Omega}^+$ can be reconstructed with a high significance as well (Figure 6).

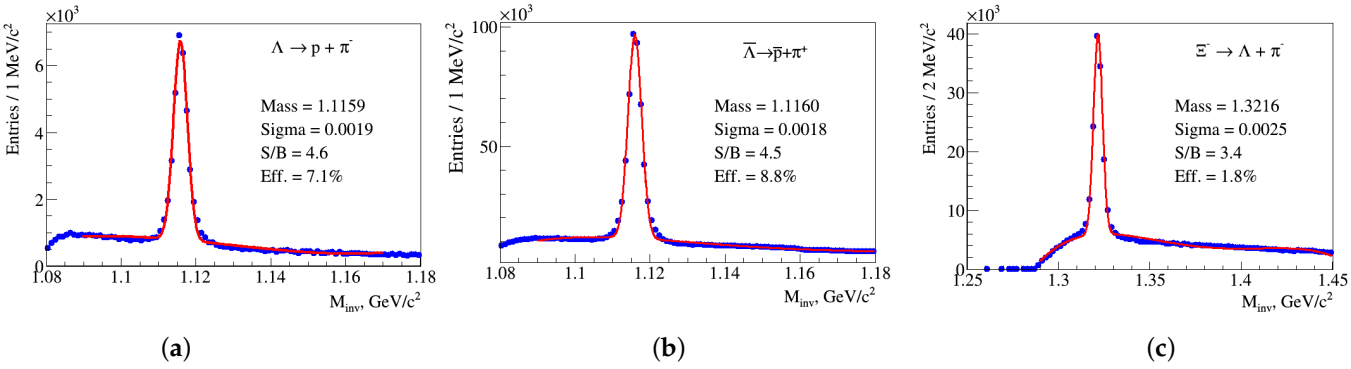

Figure 3. Reconstructed invariant mass spectra of hyperon decay products: (**a**) $\Lambda \to p + \pi^-$, (**b**) $\overline{\Lambda} \to \overline{p} + \pi^+$, (**c**) $\Xi^- \to \Lambda + \pi^-$. Results for different numbers of processed events are shown. Histograms are fitted to a sum of a Gaussian and a polynomial. The numbers in the legends present mean and sigma of the Gaussian as well as signal/background ratio and signal reconstruction efficiency, where the signal and background are calculated within $\pm 2\sigma$ interval of the peak position and efficiency is taken with respect to all hyperons produced within 50 cm of the interaction point.

In order to study light hypernuclei, the event generator DCM-QGSM [23] was used, and the decay modes and branching ratios were taken from Refs. [25,26] (Table 1) and added to the decay simulation procedures of the particle transport codes (Geant3/Geant4) with lifetimes taken to be the same as of Λ hyperon. One can see in Figure 7 that such strange objects should be visible in the experiment if sufficient event statistics are collected. The reconstructed mass values are within 1 MeV/c^2 of the ones used in the event generator, demonstrating a good self-consistency of the simulation and reconstruction procedures and a high quality of the reconstruction codes. With sufficient statistics collected, the mass determination uncertainty is expected to be dominated by the systematic effects of the real apparatus and at this stage can hardly be reliably estimated.

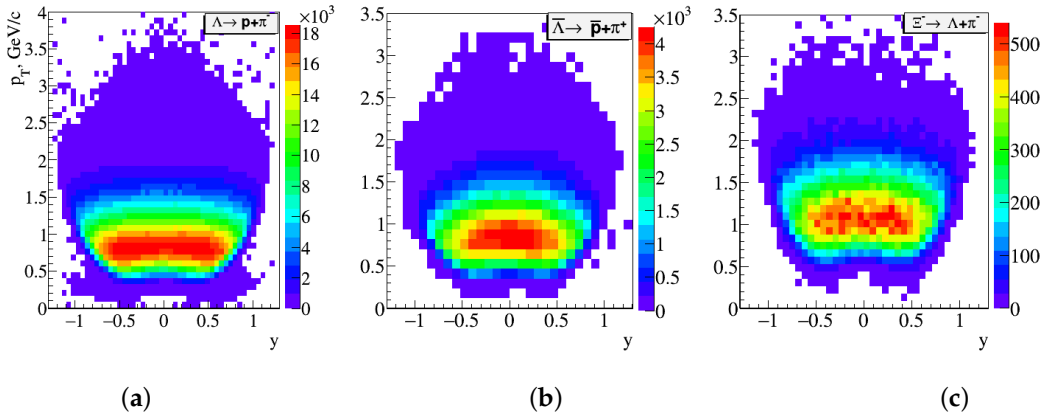

Figure 4. Transverse momentum p_T vs rapidity y phase space of reconstructed true hyperons: (**a**) Λ, (**b**) $\bar{\Lambda}$, (**c**) Ξ^-.

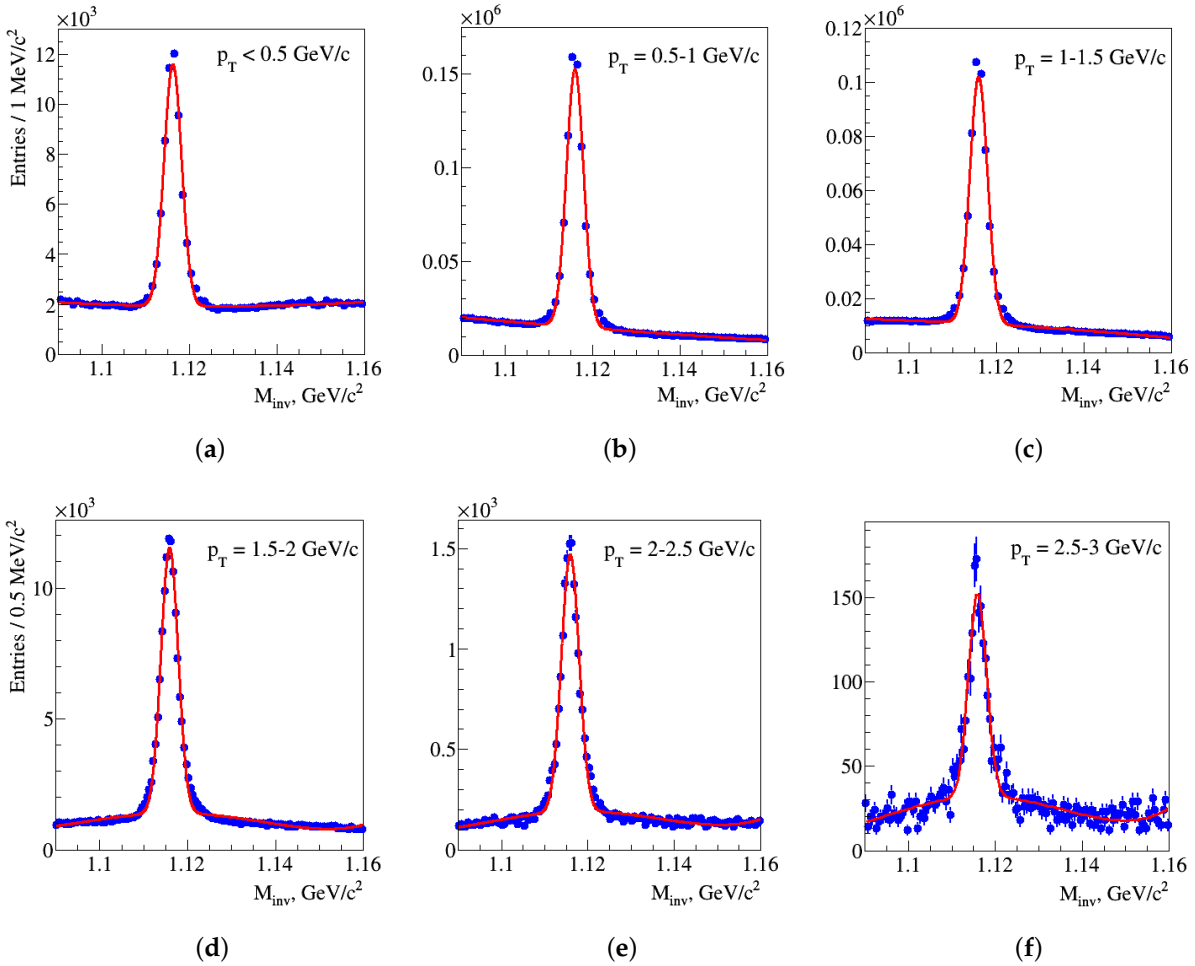

Figure 5. Reconstructed invariant mass of Λ decay products in different p_T-intervals: (**a**) $p_T < 0.5$ GeV/c, (**b**) $p_T = 0.5$–1.0 GeV/c, (**c**) $p_T = 1.0$–1.5 GeV/c, (**d**) $p_T = 1.5$–2.0 GeV/c, (**e**) $p_T = 2.0$–2.5 GeV/c, (**f**) $p_T = 2.5$–3.0 GeV/c.

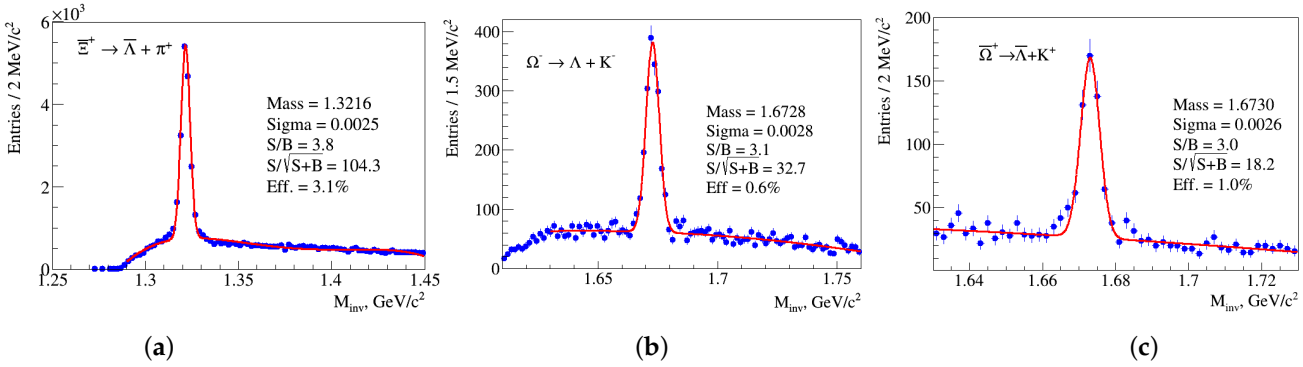

Figure 6. Reconstructed invariant mass spectra of hyperon decay products: (**a**) $\overline{\Xi}^+ \rightarrow \overline{\Lambda} + \pi^+$, (**b**) $\Omega^- \rightarrow \Lambda + K^-$, (**c**) $\overline{\Omega}^+ \rightarrow \overline{\Lambda} + K^+$. $8{\cdot}10^6$ events from PHSD [24] simulation of minimum bias Au+Au collisions at $\sqrt{s_{NN}}$ =11 GeV have been processed. Histograms are fitted to a sum of a Gaussian and a polynomial. The numbers in the legends present mean and sigma of the Gaussian as well as signal/background ratio, significance, and signal reconstruction efficiency, where the signal and background are calculated within a $\pm 2\sigma$ interval of the peak position, and efficiency is taken with respect to all hyperons produced within 50 cm of the interaction point.

Table 1. Hypernuclei decay modes and branching ratios.

Decay Channel	Branching Ratio, %
${}_{\Lambda}\mathrm{H}^3 \rightarrow \mathrm{He}^3 + \pi^-$	24.7
${}_{\Lambda}\mathrm{H}^3 \rightarrow + \mathrm{p} + \mathrm{d} + \pi^-$	36.7
${}_{\Lambda}\mathrm{H}^4 \rightarrow \mathrm{He}^4 + \pi^-$	75.0
${}_{\Lambda}\mathrm{He}^4 \rightarrow \mathrm{He}^3 + \mathrm{p} + \pi^-$	32.0

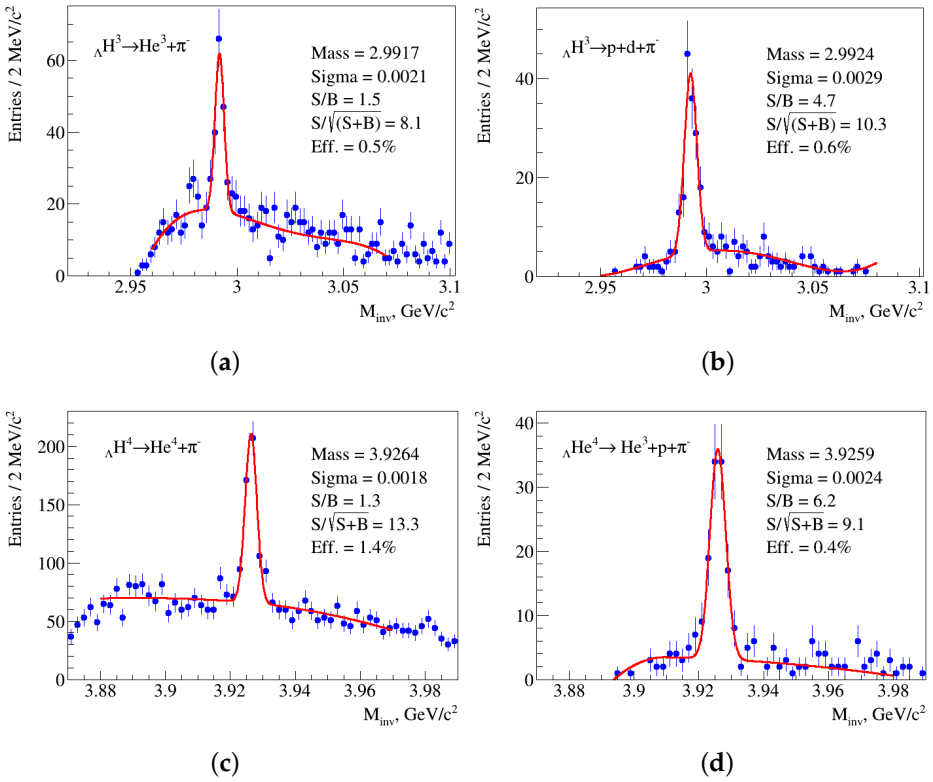

Figure 7. Reconstructed invariant mass spectra of hypernuclei decay products: (**a**) ${}_{\Lambda}H^3 \rightarrow He^3 + \pi^-$, (**b**) ${}_{\Lambda}H^3 \rightarrow p + d + \pi^-$, (**c**) ${}_{\Lambda}H^4 \rightarrow He^4 + \pi^-$, (**d**) ${}_{\Lambda}He^4 \rightarrow He^3 + p + \pi^-$. The event statistics of $9{\cdot}10^5$ for (**a**,**b**), $2{\cdot}10^7$ and $3{\cdot}10^7$ for (**c**,**d**), respectively, of central Au+Au collisions at $\sqrt{s_{NN}} = 5$ GeV from the DCM-QGSM generator [23] has been processed. Histograms are fitted to a sum of a Gaussian and a polynomial. The notations in the legends are the same as in Figure 6.

Reconstruction of short-lived strange particles from invariant mass combinations of their decay products with the approach described above has been demonstrated to be feasible as well. The examples of the observed invariant mass peaks of $\phi(1020)$ and $K^*(892)^{\pm}$ are shown in Figure 8 [27].

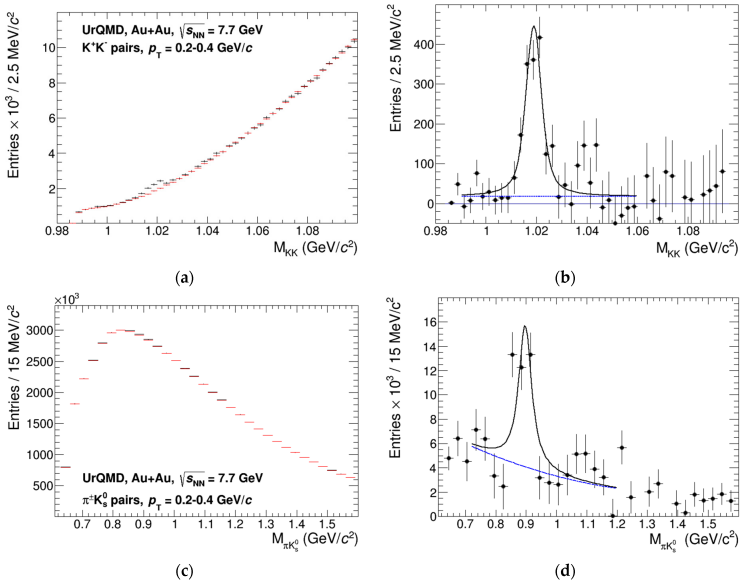

Figure 8. The invariant mass distributions accumulated for K^+K^- (**a**,**b**), and $\pi^{\pm}K^0_s$ (**c**,**d**) pairs in $5{\cdot}10^6$ Au + Au collisions at $\sqrt{s_{NN}} = 7.7$ GeV in the momentum range 0.2–0.4 GeV/c. The distributions are shown before (**a**,**c**) and after (**b**,**d**) the mixed-event background subtraction. The plots (a,c) show the foreground (black) and the mixed-event (red) invariant mass distributions (taken from Ref. [27]).

5. Conclusions

Approaches to the strange particle reconstruction developed and implemented within the software framework of the MPD experiment have been described. The results of their application during the detector Monte Carlo feasibility studies have been presented. They demonstrate reasonable selection efficiency and quality sufficient to study strangeness production in heavy-ion collisions.

Funding: This research was funded by RFBR according to the research project # 18-02-40060.

Conflicts of Interest: The funders had no role in the design of the study; in the collection, analyses, or interpretation of data; in the writing of the manuscript, or in the decision to publish the results.

References

1. Kekelidze, V.D.; Lednicky, R.; Matveev, V.A.; Meshkov, I.N.; Sorin, A.S.; Trubnikov, V.G. Three stages of the NICA accelerator complex. *Eur. Phys. J. A* **2016**, *52*, 211. [CrossRef]
2. Golovatyuk, V.; Kekelidze, V.; Kolesnikov, V.; Rogachevsky, O.; Sorin, A. The multi-purpose detector (MPD) of the collider experiment. *Eur. Phys. J. A* **2016**, *52*, 212. [CrossRef]
3. Antinori, F.; Bacon, P.A.; Badala, A.; Barbera, R.; Belogianni, A.; Bloodworth, I.J.; Bombara, M.; Bruno, G.E.; Bull, S.A.; Caliandro, R.; et al. [NA57 Collaboration.] Strangeness enhancements at central rapidity in 40 A GeV/c Pb–Pb collisions. *J. Phys. G* **2010**, *37*, 045105.
4. Abelev, B.I.; Aggarwal, M.M.; Ahammed, Z.; Anderson, B.D.; Arkhipkin, D.; Averichev, G.S.; Bai, Y.; Balewski, J.; Barannikova, O.; Barnby, L.S.; et al. [STAR Collaboration] Enhanced strange baryon production in Au+Au collisions compared to p + p at $\sqrt{s_{NN}}$ = 200 GeV. *Phys. Rev. C* **2008**, *77*, 044908. [CrossRef]
5. Rafelski, J.; Muller, B. Strangeness production in the quark–gluon plasma. *Phys. Rev. Lett.* **1982**, *48*, 1066. [CrossRef]
6. Becattini, F.; Manninen, J. Centrality dependence of strangeness production in heavy-ion collisions as a geometrical effect of core-corona superposition. *Phys. Lett. B* **2009**, *673*, 19–23. [CrossRef]
7. Most, E.R.; Papenfort, L.J.; Dexheimer, V.; Hanauske, M.; Schramm, S.; Stöcker, H.; Rezzolla, L. Signatures of Quark-Hadron Phase Transitions in General-Relativistic Neutron-Star Mergers. *Phys. Rev. Lett.* **2019**, *122*, 061101. [CrossRef] [PubMed]
8. Kerman, A.K.; Weiss, M.S. Superstrange Nuclei. *Phys. Rev. C* **1973**, *8*, 408. [CrossRef]

9. Wakai, M.; Bando, H.; Sano, M. Hypernucleus Formation in High-energy Nuclear Collisions. *Phys. Rev. C* **1998**, *38*, 748. [CrossRef] [PubMed]
10. Andronic, A.; Braun-Munzinger, P.; Stachel, J.; Stocker, H. Production of light nuclei, hypernuclei and their antiparticles in relativistic nuclear collisions. *Phys. Lett. B* **2011**, *697*, 203–207. [CrossRef]
11. Steinheimer, J.; Gudima, K.; Botvina, A.; Mishustin, I.; Bleicher, M.; Stocker, H. Hypernuclei, dibaryon and antinuclei production in high energy heavy ion collisions: Thermal production versus Coalescence. *Phys. Lett. B* **2012**, *714*, 85–91. [CrossRef]
12. Riabov, V. Short-Lived Resonances as Probes of the Medium Produced in Heavy-Ion Collisions. *Particles* **2020**, *4*, 1. [CrossRef]
13. Abraamyan, K.U.; Afanasiev, S.V.; Alfeev, V.S.; Anfimov, N.; Arkhipkin, D.; Aslanyan, P.Z.; Babkin, V.A.; Baznat, M.I.; Bazylev, S.N.; Blaschke, D.; et al. [MPD Collaboration] The MPD detector at the NICA heavy-ion collider at JINR. *Nucl. Instrum. Methods A* **2011**, *628*, 99–102. [CrossRef]
14. Luchsinger, R.; Grab, C. Vertex reconstruction by means of the method of Kalman filter. *Comput. Phys. Commun.* **1993**, *76*, 263–280. [CrossRef]
15. Gertsenberger, K.; Merts, S.; Rogachevsky, O.; Zinchenko, A. Simulation and analysis software for the NICA experiments. *Eur. Phys. J. A* **2016**, *52*, 214. [CrossRef]
16. Gorbunov, S.; Kisel, I. Reconstruction of decayed particles based on the Kalman filter. *CBM SOFT Note 2007 003* **2007**, *7*. Available online: https://www.star.bnl.gov/~bouchet/KFParticle/DOC-2007-May-14-1.pdf (accessed on 21 April 2021) .
17. Hulsbergen, W.D. Decay chain fitting with a Kalman filter. *Nucl. Instrum. Meth. A* **2005**, *552*, 566–575. [CrossRef]
18. Ilieva, M.; Kolesnikov, V.; Murin, Y.; Suvarieva, D.; Vasendina, V.; Zinchenko, A.; Litvinenko, E.; Gudima, K. Evaluation of the MPD Detector Capabilities for the Study of the Strangeness Production at the NICA Collider. *Phys. Part. Nucl. Lett.* **2015**, *12*, 100–112. [CrossRef]
19. Ilieva, M.; Kolesnikov, V.; Suvarieva, D.; Vasendina, V.; Zinchenko, A. Reconstruction of Multistrange Hyperons with the MPD Detector at the NICA Collider: a Monte Carlo Feasibility Study. *Phys. Part. Nucl. Lett.* **2015**, *12*, 618–627. [CrossRef]
20. Drnojan, J.; Levterova, E.; Vasendina, V.; Zinchenko, A.; Zinchenko, D. Perspectives of Multistrange Hyperon Study at NICA/MPD from Realistic Monte Carlo Simulation. *Phys. Part. Nucl. Lett.* **2020**, *17*, 32–43. [CrossRef]
21. Kolesnikov, V.I.; Zinchenko, A.I.; Vasendina, V.A. Prospects for Studying Hyperons and Hypernuclei on the NICA Collider. *Bull. Russ. Acad. Sci. Phys.* **2020**, *84*, 451–454. [CrossRef]
22. Bass, S.A. Microscopic models for ultrarelativistic heavy ion collisions. *Prog. Part. Nucl. Phys.* **1998**, *41*, 255–369. [CrossRef]
23. Toneev, V.D.; Amelin, N.S.; Gudima, K.K.; Sivoklokov, S.Y. Dynamics of relativistic heavy ion collisions. *Nucl. Phys. A* **1990**, *519*, 463–478. [CrossRef]
24. Cassing, W.; Bratkovskaya, E.L. Parton-hadron-string dynamics: An off-shell transport approach for relativistic energies. *Nucl. Phys. A* **2009**, *831*, 215–242. [CrossRef]
25. Kamada, H.; Golak, J.; Miyagawa, K.; Witala, H.; Gloeckle, W. Pi mesonic decay of the hypertriton. *Phys. Rev. C* **1998**, *57*, 1595. [CrossRef]
26. Kumagai-Fuse, I.; Okabe, S.; Akaishi, Y. Pionic decay spectra of few body Lambda hypernuclei. *Phys. Rev. C* **1996**, *54*, 2843. [CrossRef]
27. Ivanishchev, D.; Kotov, D.; Malaev, M.; Riabov, V.; Ryabov, Y. Resonance Reconstruction in the MPD. *Particles* **2021**, *4*, 3. [CrossRef]